

Time-resolved molecular non-equilibrium spectra in nanosecond laser induced air plasma

Xuteng Zhang(张续腾), Chaobo Yang(杨超博), Xun Yuan(袁勋), Minghong Han(韩明宏), Zhen Cao(曹振), Jiangbo Peng(彭江波), and Xin Yu(于欣)

Citatio: Chin. Phys. B, 2025, 34 (**9**): 094701. DOI: 10.1088/1674-1056/ade24a
http://cpb.iphy.ac.cn; http://iopscience.iop.org/cpb

What follows is a list of articles you may be interested in

Numerical simulation of the thermal non-equilibrium flow-field characteristics of a hypersonic Apollo-like vehicle

Minghao Yu(喻明浩)†, Zeyang Qiu(邱泽洋), Bo Lv(吕博), and Zhe Wang(王哲)
Chin. Phys. B, 2022, 31 (**9**): 094702. DOI: 10.1088/1674-1056/ac6ed6

Effects of single synthetic jet on turbulent boundary layer

Jin-Hao Zhang(张津浩), Biao-Hui Li(李彪辉), Yu-Fei Wang(王宇飞), and Nan Jiang(姜楠)
Chin. Phys. B, 2022, 31 (**7**): 074702. DOI: 10.1088/1674-1056/ac4bd0

Flow separation control over an airfoil using continuous alternating current plasma actuator

Jian-Guo Zheng(郑建国)
Chin. Phys. B, 2021, 30 (**3**): 034702. DOI: 10.1088/1674-1056/abd466

Aerodynamic actuation characteristics of radio-frequency discharge plasma and control of supersonic flow

Zhen Yang(杨臻), Hui-Min Song(宋慧敏), Hong-Yu Wang(王宏宇), Shan-Guang Guo(郭善广), Min Jia(贾敏), Kang Wang(王康)
Chin. Phys. B, 2019, 28 (**2**): 024701. DOI: 10.1088/1674-1056/28/2/024701

Coherent structures over riblets in turbulent boundary layer studied by combining time-resolved particle image velocimetry (TRPIV), proper orthogonal decomposition (POD), and finite-time Lyapunov exponent (FTLE)

Shan Li(李山), Nan Jiang(姜楠), Shaoqiong Yang(杨绍琼), Yongxiang Huang(黄永祥), Yanhua Wu(吴彦华)
Chin. Phys. B, 2018, 27 (**10**): 104701. DOI: 10.1088/1674-1056/27/10/104701

Time-resolved molecular non-equilibrium spectra in nanosecond laser induced air plasma

Xuteng Zhang(张续腾)[1,2], Chaobo Yang(杨超博)[1,2,†], Xun Yuan(袁勋)[1,2], Minghong Han(韩明宏)[1,2], Zhen Cao(曹振)[1,2,‡], Jiangbo Peng(彭江波)[1,2], and Xin Yu(于欣)[1,2]

[1] *National Key Laboratory of Laser Spatial Information, Harbin Institute of Technology, Harbin* 150001, *China*
[2] *Institute of Opt-electronics, Harbin Institute of Technology, Harbin* 150001, *China*

(Received 5 March 2025; revised manuscript received 3 June 2025; accepted manuscript online 9 June 2025)

We performed a quantitative analysis of time-resolved laser-induced breakdown air plasma spectra to obtain the evolution of temperatures and species relative fractions. The air plasma was generated by focusing a 100 mJ Nd:YAG laser pulse, and the time-resolved spectra were recorded by an intensified charge-coupled device camera with incremental delay. The attention was mainly focused on the emission spectra of the first negative system of nitrogen (N_2^+, $B^2\Sigma_u^- – X^2\Sigma_g^+$) and the violet system of carbon nitride (CN, $B^2\Sigma^+ – X^2\Sigma^+$) located at 383–396 nm. A custom-built model was developed to perform the simulation and fitting of the N_2^+ and the CN spectra from the air plasma. The model was verified by comparing to a published model with a 0.9860 Spearman correlation coefficient. With this model, the time-resolved non-equilibrium temperatures and relative fractions of N_2^+ and CN were obtained with a fitting correlation coefficient higher than 0.9108.

Keywords: non-equilibrium, time-resolved, diatomic molecule, optical emission spectroscopy

PACS: 47.70.Nd, 52.25.Tx, 33.20.–t, 02.70.Hm

DOI: 10.1088/1674-1056/ade24a **CSTR:** 32038.14.CPB.ade24a

1. Introduction

Non-equilibrium flow is an active research area.[1] It has enormous potential applications in various disciplines, particularly in aerospace and military contexts.[2–7] The surface flow of a hypersonic vehicle at high altitude is essentially in a thermodynamic non-equilibrium state. The thermodynamic and aerodynamic properties of non-equilibrium flow significantly impact the design of thermal protection systems and aerodynamic structures.[8] So far, there has been extensive research on non-equilibrium states. Many classical models have also been developed, which describe the thermochemical non-equilibrium processes for spacecraft entry into the Earth's atmosphere.[9,10] However, the complexity of non-equilibrium states has led to limitations in these models. Spectroscopy can directly obtain the particle population distribution at various energy levels and internal energy distribution within non-equilibrium molecular systems,[11] thus better characterizing the thermodynamic and aerodynamic properties of non-equilibrium flow, which has gradually garnered wide attention from researchers. Optical emission spectroscopy (OES),[12–16] in particular, had been employed to carry out experimental analysis of plasmas, since its non-intrusive nature and ability to access more information concerning plasmas. Non-equilibrium spectra of plasmas were obtained using OES, and the researchers estimated their vibrational and rotational temperatures.[3,17–20]

NASA observed the phenomenon of high-level overpopulation at the IHF Arc Jet Facility,[21] where the particle number distribution no longer adhered to the Boltzmann distribution. However, the spectral resolution obtained by NASA was relatively low. Subsequently, higher-resolution strongly non-equilibrium spectra were gradually obtained internationally under different experiment setups and conditions.[22–26] Michael W. Winter proposed a fitting method that introduced an overpopulation factor N_{over}[27] to analyze non-equilibrium spectra that do not satisfy the Boltzmann distribution, which significantly enhanced the alignment of line profile and intensity between the fitted and measured spectra. In summary, two types of population distributions can be used to analyze the non-equilibrium state: the Boltzmann distribution with different vibrational and rotational temperatures, and the non-Boltzmann distribution. Researchers around the world have conducted a large number of plasma spectral measurement experiments and carried out corresponding analyses and temperature extractions.

In this work, time-resolved spectra of CN and N_2^+ from laser induced breakdown plasma were measured. We developed a model for the simulation and fitting of the N_2^+ and the CN spectra. Based on the Boltzmann model, the temporal evolution of the rovibrational temperatures, T_v and T_r, and the relative fractions of N_2^+ and CN were obtained. The approach presented in this work has the potential to be applied

†Corresponding author. E-mail: yangchaobo@hit.edu.cn
‡Corresponding author. E-mail: caozhen1995@hit.edu.cn

© 2025 Chinese Physical Society and IOP Publishing Ltd. All rights, including for text and data mining, AI training, and similar technologies, are reserved.

in the analysis of non-equilibrium emission spectra, including non-Boltzmann distribution spectra.

2. Experiment and method

2.1. Experiment

Figure 1 is the schematic of the experiment setup. In this work, we utilized a plasma-generation system similar to that in previous studies.[28–31] Specifically, a Nd:YAG laser (Surelite, SL II-10), with a laser output of 10 Hz at 532 nm and the maximum energy of 230 mJ, was employed. A 50 mm focal lens was employed to focus the laser, ensuring it has sufficient energy to break down air. To minimize optical losses and improve collection efficiency, a UV prime lens (Jenoptik, UV CoastalOpt SLR objective lens, $f = 105$ mm, $f/4.5$) was used to collect and image the air plasma spectrum in the spectrometer slit ($F = 500$ mm). The spectra dispersed by the spectrometer were recorded by an intensified charge-coupled device (ICCD) camera. We set the laser intensity to 100 mJ and the slit width of the spectrometer to 100 μm, with a grating line density of 1800 lines/mm, which was able to obtain spectra with a higher resolution compared to previous work.[19,20,32] The digital delay generator (Stanford Research Systems, DG645) can set the acquisition time and exposure time of the ICCD camera, enabling the camera to accurately capture the non-equilibrium spectral signals. The ICCD was set to integrate 0.1 μs per acquisition and accumulate 200 counts per readout, which was conducive to obtaining signals with a relatively high signal-to-noise ratio.

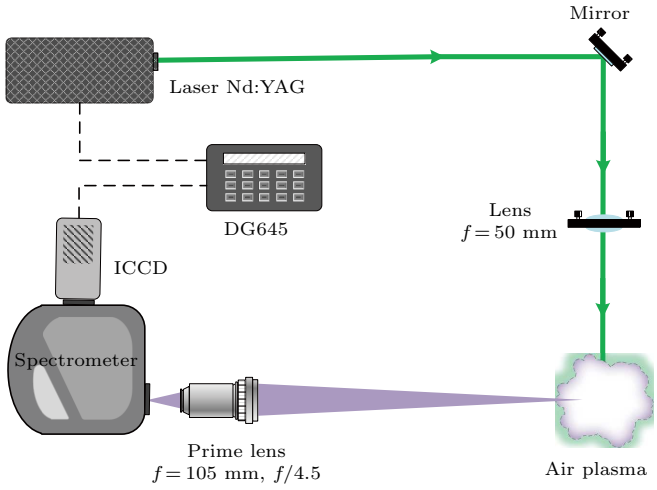


Fig. 1. Experiment setup schematic.

The mechanism of laser-induced plasma generation indicates that during the initial stage of plasma formation, continuous background radiation plays a predominant role. As the temperature decreases, this radiation gradually diminishes, and electronic transitions within atoms become more active, leading to the emergence of the atomic spectrum. As the temperature continues to drop, electrons, ions, and atoms recombine to form molecules or molecular ions, resulting in the spectrum dominated by molecules.[33] In addition, the molecular state is characterized as non-equilibrium due to the influence of high temperatures and shock waves in the early stage of molecular formation. As collisions between molecules persist, the system gradually approaches an equilibrium state. Therefore, the detection time was critical for this experiment. We initially set the acquisition time interval to 5 μs to estimate the generation times of the plasma spectra at various stages. After that, we adjusted the acquisition time interval to 1 μs and conducted precise time-resolved measurements on the spectra in the initial stage of molecular generation, focusing on the wavelength range from 383 nm to 396 nm, to capture the non-equilibrium spectra of N_2^+ and the CN. At the end of the experiment, a mercury lamp was used to measure the spectral resolution at the 100 μm entrance slit, using a 404.7 nm reference peak approximated by a Voigt function with a 0.087 nm FWHM (full width at half maximum). This latter feature represents the slit function, which was used to convolve the theoretical spectra for comparison with the measurement.

2.2. Simulation

According to Herzberg's analysis of the rovibrational energy of diatomic molecules,[34] the vibrational and rotational energy considering the coupling of rovibrational energy are as follows:

$$F_v(J) = B_v J(J+1) - D_v J^2(J+1)^2, \tag{1}$$

$$G(v) = \omega_e(v+1/2) - \omega_e x_e(v+1/2)^2, \tag{2}$$

where v and J represent the vibrational and rotational levels, respectively. B_v and D_v are rotational and centrifugal distortion constants. For a specific electronic system, the spontaneous emission intensity of non-equilibrium molecule, based on Boltzmann distribution,[35] can be expressed as

$$I = C_0 \Phi \sigma^4 \frac{1}{Q} \exp\left[-\frac{G(v')}{T_v} - \frac{F(v',J')}{T_r}\right] \times q_{v'v''} |R_e(r_{v'v''})|^2 S_{J'J''}, \tag{3}$$

where σ is the wavenumber with the expression

$$\sigma = \Delta T_e + G(v') - G(v'') + F(J') - F(J''), \tag{4}$$

where T_v and T_r are the rovibrational temperatures. Φ represents the nuclear spin factor, which is related to the parity of J. Q is the total partition function. $q_{v'v''}$ is the Franck–Condon factor between vibrational levels and $R_e(r_{v'v''})$ are electronic transition moment functions, both of which are accessible constants. $S_{J'J''}$ is the Hönl–London factor related to the difference in the components of the orbital angular momentum between the upper and lower electronic levels.

Table 1. Klein–Dunham coefficients of N_2^+.[36]

Klein–Dunham coefficients (cm^{-1})	$B^2\Sigma_u^-$	$X^2\Sigma_g^+$
T_e	25467.025	0
ω_e	2406.67	2197.95
$\omega_e x_e$	23.3782	16.0906
B_e	2.07492	1.92286
α_e	0.02088	0.0186
D_e	6.1912×10^{-6}	5.8866×10^{-6}
β_e	1.3882×10^{-6}	3.3812×10^{-6}

In the following, the N_2^+ first negative system ($B^2\Sigma_u^-$–$X^2\Sigma_g^+$) is taken as an example for simulation. Deheng Shi *et al.* re-evaluated the Klein–Dunham coefficients of N_2^+, as shown in Table 1.[36]

Based on Eqs. (1)–(4), the spectral constants in Table 1, and the selection rules for transitions, the theoretical spectra can be obtained, which are the stick spectra containing information on line intensities and line positions. During these calculations, we defined the rotational quantum numbers as $J = 0,1,2,3,\ldots,150$ and the vibrational quantum numbers as $v = 0,1,2,3,4$, then mapped all relevant parameters into their respective two-dimensional matrices associated with vibration-rotation quantum numbers, such as the rotational energy matrix ($\boldsymbol{F} \in \mathbb{R}^{5\times151}$) and the upper-level population matrix ($\boldsymbol{Q}' \in \mathbb{R}^{5\times151}$), and the line positions and line intensities were calculated using a vectorized approach, which significantly improves the calculation speed of theoretical spectra. After the theoretical spectra are equally spaced, convolving them with the slit function obtained in Subsection 2.1 can yield the final simulated spectra. Figure 2 compares the spectra obtained from the simulation code with the spectra by the SPECAIR,[37–39] which was developed at Stanford based on the NASA NEQAIR code and is based on accurate spectroscopic database. The purple line represents the simulated spectra, while the brown line represents the SPECAIR results. Figure 2(a) shows the comparison of the results for a rovibrational temperature $T_v = T_r = 2000$ K , corresponding to the equilibrium state. Figure 2(b) shows the comparison for $T_v = 5000$ K, $T_r = 3000$ K, corresponding to the non-equilibrium state. It is clear that the line positions of each band match well, and the overall similarity of each band is good under the condition of approximately equal peak values. On the other hand, the line shapes of each band also have a high degree of matching. Furthermore, the dark green box shows detailed comparison of certain bands, where it is evident that the wavelength ranges match, the line position coincides, and the intensity distributions and line shapes at different wavelengths are approximately overlapping. We also used the Spearman coefficient[40] to quantitatively evaluate the correlation between the simulation and SPECAIR. The formula is given as

$$\rho = 1 - \frac{6\sum d_i^2}{n(n^2-1)}, \tag{5}$$

where d_i represents the difference in rank values of the i-th data pair. n is total sample size. Generally speaking, the closer the value is to 1 (or -1), the higher the correlation will be. Additionally, correlations are classified as strong when the absolute value of the correlation coefficient exceeds 0.7, moderate when it falls between 0.4 and 0.7, and weak when it ranges from 0 to 0.4.[41,42] The Spearman correlation coefficient is 0.9921 for the former, while for the latter it is 0.9860, which means that the simulation outcome is satisfactory. It is noted that the simulation model developed in this paper has a high calculation rate, which can significantly improve the fitting efficiency of the fitting procedure described below and is highly valuable for processing large batches of spectra.

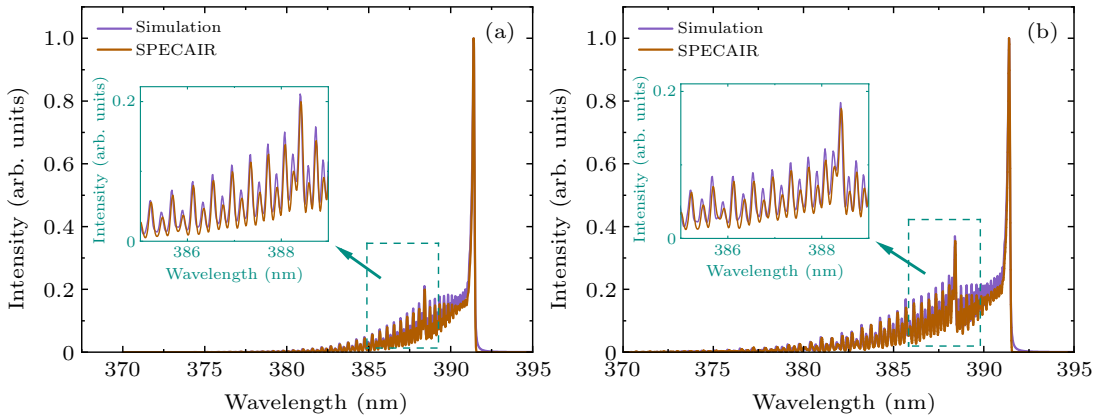


Fig. 2. Comparison diagram of N_2^+ with different rovibrational temperatures: (a) $T_v = T_r = 2000$ K, the inset is a partial enlarged view of the wavelength range from 385 nm to 389 nm. (b) $T_v = 5000$ K, $T_r = 3000$ K, the inset is a partial enlarged view of the wavelength range from 385 nm to 389 nm.

2.3. Fitting procedure

According to Eq. (3), intensity I could be regarded as a function of the rovibrational temperatures, T_v and T_r. In other words, the spectral simulation model described in Subsection 2.2 would serve as the simulation function SIM$(\cdot)$ for vibrational–rotational temperature retrieval. The parameter

PARM for the SIM is a list, including the vibrational temperature T_r, rotational temperature T_v, and wavelength measurement error $\Delta\lambda_{\text{shift}}$. By using T_v and T_r as fitting parameters, a series of numerical simulations of molecular spectra corresponding to different rovibrational temperatures are calculated. These simulated spectra are then matched with the measured spectra. Therefore, the optimal temperature is obtained, optimizing the fitting parameters through the least squares method (LSM).[43] The flowchart of the fitting procedure is illustrated in Fig. 3.

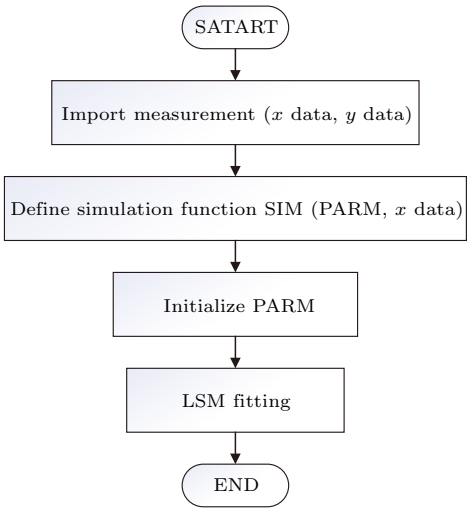


Fig. 3. The flowchart of least squares fitting for vibrational temperature and rotational temperature.

To validate the accuracy of the fitting code theoretically, Gaussian noise similar to the experimental noise was superimposed on the simulated spectrum to serve as the measured spectrum for fitting.[44] Meanwhile, we conducted an initial value randomness test on this fitting procedure; that is, the similar fitting temperature can be obtained by randomly generating initial values. Figure 4 shows the comparison of the fitting result with the measured spectrum, with the dark green box highlighting the detailed comparison of certain bands, which indicates that the result is consistently very close to the measurement. In terms of fitting values, the rovibrational temperatures of measured spectrum are 2000 K and 1000 K, respectively, and the fitting results show the vibrational temperature of 1974.35 K and the rotational temperature of 1004.98 K.

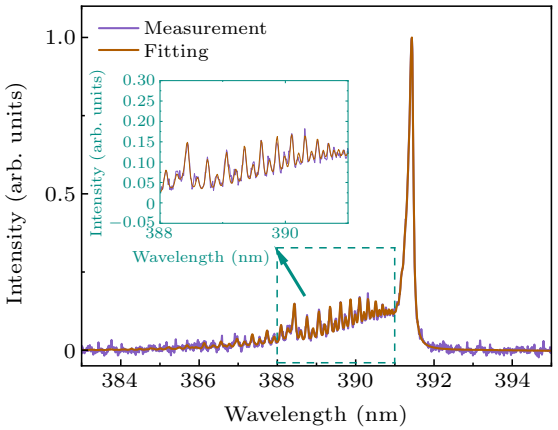


Fig. 4. Comparison diagram between the fitting spectrum and the spectrum with noise, where the vibrational temperature is 2000 K and the rotational temperature is 1000 K, the inset is a partial enlarged view of the wavelength range from 388 nm to 391 nm.

3. Result and discussion

Figure 5 shows the plasma spectra measured at different detection times, with the plasma generation moment defined as

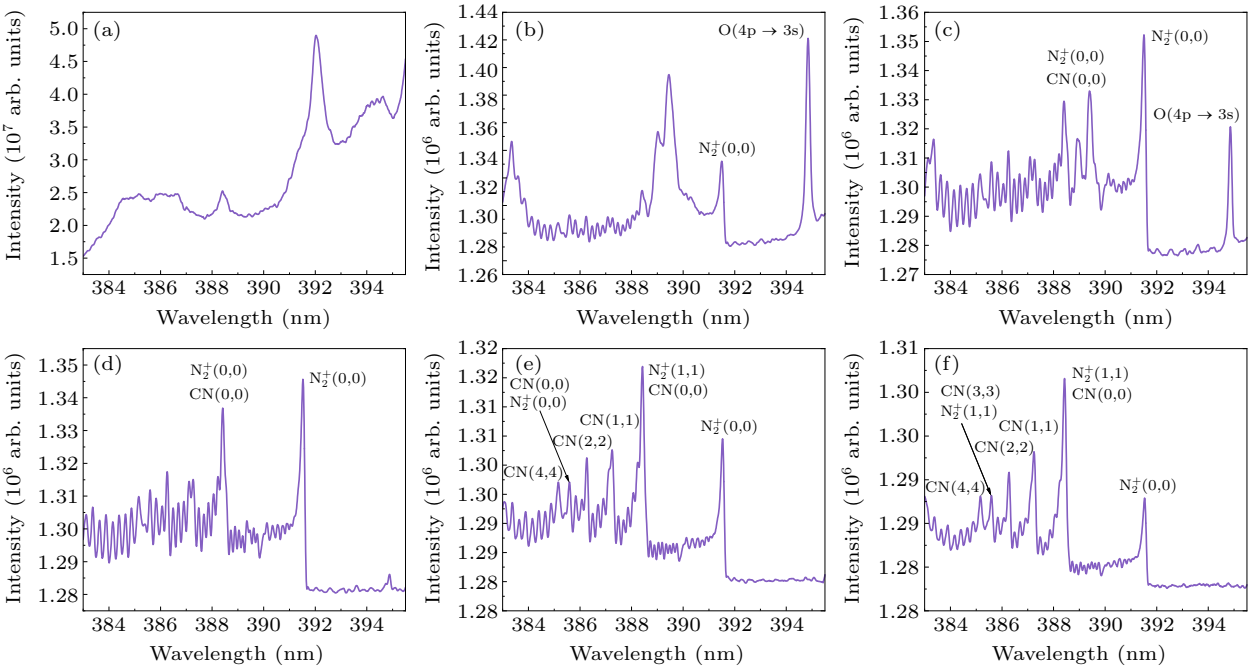


Fig. 5. Nanosecond laser induced air plasma spectra at different times: (a) $t = 0$ μs, continuum radiation spectrum, (b) $t = 5$ μs, spectrum with continuous radiation and atomic–molecular radiation, (c) $t = 10$ μs, atomic–molecular spectrum, (d) $t = 15$ μs, atomic–molecular spectrum, (e) $t = 20$ μs, molecular spectrum, (f) $t = 25$ μs, molecular spectrum.

$t = 0$ μs. At that moment, the emission spectrum was mainly characterized by continuum radiation. The continuum radiation has strongly decreased at $t = 5$ μs; in addition, a band spectrum with a peak at 391.4 nm and a discrete spectrum with a peak at 394.8 nm has appeared, corresponding to the N_2^+ first negative system ($B^2\Sigma_u^- – X^2\Sigma_g^+$), (0,0) band and the O (4p–3s) spectra line, respectively. Until $t = 15$ μs, the discrete spectral line has disappeared, leaving only the band spectrum, indicating that molecular radiation dominates. At $t = 20$ μs, the CN violet system ($B^2\Sigma^+ – X^2\Sigma^+$) appeared with two peaks at 387.3 nm and 386.3 nm.

To further analyze the time evolution characteristics of the N_2^+ and CN, the emission spectra were recorded at intervals of 1 μs, with 10 acquisitions being made at each moment, and the measurements are presented in Fig. 6. Evidently, the radiation intensity of O(4p–3s) exhibits a gradual decline and reaches zero at 15 μs. As stated previously, temperature information reflected in the measured spectra can be extracted through spectral simulation and LSM fitting. Since there are two electronic transition systems in the measured spectra, N_2^+ and CN, the intensities I from Eq. (3) of both should be multiplied by their respective proportionality coefficients a and b, and the intensity, I_{new}, is given by

$$I_{\text{new}} = a \times I_{N_2^+} + b \times I_{\text{CN}}. \tag{6}$$

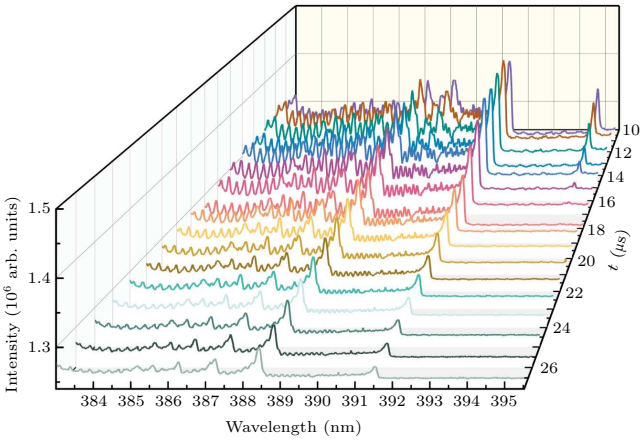


Fig. 6. Molecular spectra of air plasma at 1 μs intervals with 10-time accumulations per microsecond.

The simulation obtained using this method serves as the fitting function, and we fit the measured spectra through the LSM. The fitting spectra and the measurements are shown in Fig. 7. It is important to note that there is an unknown peak in the measured spectrum at $t = 10$–15 μs, in the 389–390 nm range, which led to the exclusion of this portion from the fitting process. The fitting spectra match the measurement results well both in terms of line profile and intensity, and the Spearman correlation coefficient is 0.9250 for 14 μs, while for 19 μs it is 0.9419. Moreover, these values at other instants are all greater than 0.9108, and the fitting results show a good agreement, indicating that the molecules in the plasma still follow the Boltzmann distribution, with only the vibrational and rotational temperatures differing.

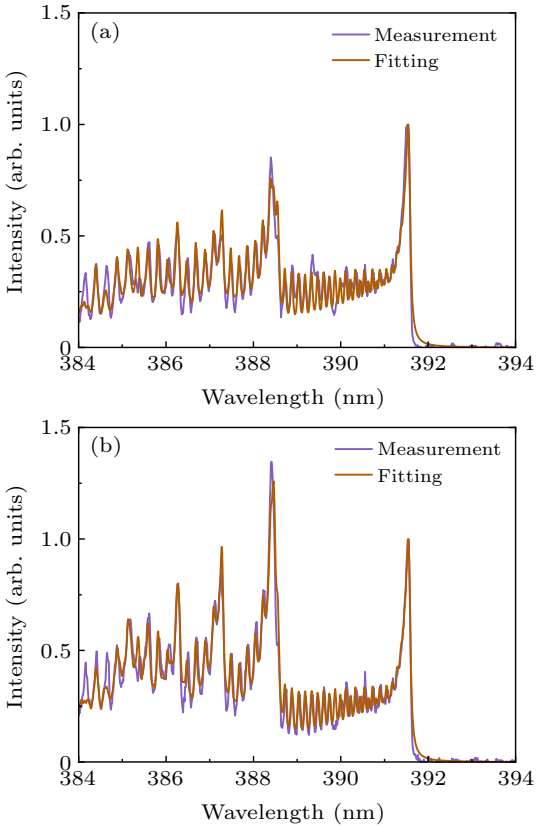


Fig. 7. Comparison diagram of fitting spectra and measured spectra at different times: (a) $t = 14$ μs and (b) $t = 19$ μs.

Using the aforementioned method to fit the measured spectra from 10 μs to 26 μs, the temporal evolution patterns of the relative fractions of N_2^+ and CN, as well as the rovibrational temperatures, were obtained. In fact, only the ratio of the fitting parameters a and b is meaningful, as it arose from normalization during the fitting process. The following conversion is necessary to proceed:

$$\begin{cases} a_1(t) = a_0(t) \times I_{\text{nor}}(t)/a_0(t), \\ b_1(t) = b_0(t) \times I_{\text{nor}}(t)/a_0(t), \\ a(t) = a_1(t)/a_1(t = 10\ \mu\text{s}), \\ b(t) = b_1(t)/a_1(t = 10\ \mu\text{s}), \end{cases} \tag{7}$$

where a_0 and b_0 are the fitting results, and $I_{\text{nor}}(t)$ is the normalization factor during the fitting process. As illustrated in Fig. 8(a), N_2^+ exhibits a trend of initially increasing followed by a decrease. The relative fraction of N_2^+ peaks at 12 μs and then begins to decline, with its second derivative also exhibiting an initial increase followed by a decrease, leading to a rapid decline of N_2^+ between 14 μs and 18 μs. In contrast, the overall change of the relative fraction of CN is not significant. It slowly decreases after approximately $t = 15$ μs. At 26 μs, the relative fraction of N_2^+ decreases to approximately 0.0645 of its maximum value, indicating that a significant amount of N_2^+ has converted to other species.

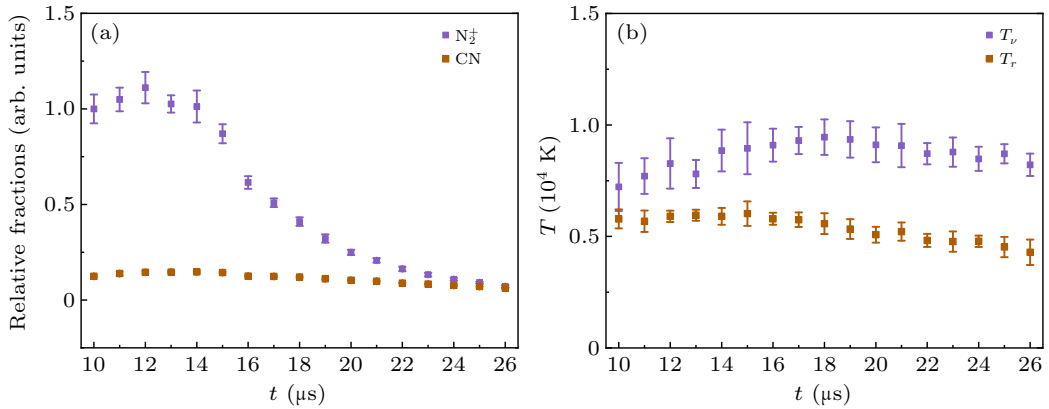


Fig. 8. The results obtained by fitting the time-resolved measurement spectra: (a) Time-resolved relative fractions of N_2^+ and CN. (b) Time-resolved rovibrational temperatures of N_2^+ and CN.

Figure 8(b) presents the time variation of rotational and vibrational temperature. The error bars represent the standard deviation derived from 10 repeated measurements at each time point, reflecting the reproducibility of measurement results. Regarding the rotational temperature, the error bars are noticeably short, indicating results are more precise. Besides, it shows a gradual decreasing trend after 15 μs, with only slight variation, and the rate is approximately 136.70 K/μs, which means that the rotational temperature might reach equilibrium through collisions. For vibrational temperature T_V, it first increases, peaks around 18 μs, and then decreases gradually. However, the error bars are relatively large, indicating a higher uncertainty in the vibrational temperature, especially in the early stages (10–14 μs) and near the peak. Certainly, at this stage, the vibrational temperature and rotational temperature are not the same, which can be determined that the molecules are in a non-equilibrium state.

4. Conclusion and outlook

This paper has carried out high-resolution time-resolved measurements on CN and N_2^+ in air plasma and conducted quantitative analysis. We have developed a custom-built model to perform the simulation and fitting of the N_2^+ and the CN spectra. After fitting the measured spectra using the Boltzmann distribution with different vibrational and rotational temperatures, the results demonstrated a high-quality match in both line profile and intensity between the fitting results and the measured with the Spearman correlation coefficient not less than 0.9108, indicating that the molecules are in non-equilibrium state. Additionally, the temporal evolution of the relative fraction and rovibrational temperatures, T_V and T_r, for N_2^+ and CN were obtained: (i) The relative fractions of N_2^+ first increases and then decreases. The overall change of the relative fraction of CN is not significant. (ii) T_V first increases and then slowly decreases, but T_r declines monotonically at a rate of 136.70 K/μs, leading to a non-monotonic variation in the population.

This model can also extract the population from molecular spectra that do not follow the Boltzmann distribution (non-Boltzmann distribution). Future work will concentrate on spectral measurements in ground wind tunnels, utilize appropriate distribution laws to extract the population state, and build a comprehensive experimental database, aiming to provide strong support and a basis for improving the numerical models used to simulate the hypersonic flow fields.

Acknowledgment

Project supported by the National Natural Science Foundation of China (Grant No. 62305087).

References

[1] Bruggeman P J, Sadeghi N, Schram D C and Linss V 2014 *Plasma Sources Sci. Technol.* **23** 023001
[2] Wysong I J, Gimelshein S F, Bykova N E, Shatalov O P and Zabelinski I E 2019 *31st International Symposium on Rarefied Gas Dynamics (RGD)*, 2023, Melville, America, p. 180008
[3] Sintsov S, Tabata K, Mansfeld D, Vodopyanov A and Komurasaki K 2020 *J. Phys. D-Appl. Phys.* **53** 305203
[4] Holloway M E, Hanquist K M and Boyd I D 2020 *J. Thermophys. Heat Transf.* **34** 538
[5] Holloway M E, Chaudhry R S and Boyd I D 2022 *J. Spacecr. Rockets* **59** 389
[6] Jans E, Lynch K P, Daniel K, Downing C, Wagner J L, Wagnild R,Maeng J B and Kearney S P 2023 *AIAA SCITECH 2023 Forum*, January1, 2023, National Harbor,America
[7] Wang W, Sun S, Li J, Zheng D, Huang S, Tian H, Yang H and Li J 2023 *Chin. Phys. B* **33** 010701
[8] Uyanna O and Najafi H 2020 *Acta Astronaut.* **176** 341
[9] Park C, Howe J, Jaffe R and Candler G 1991 29*th Aerospace Sciences Meeting*, January 1, 1991, Reno, America
[10] Kang S, Dunn M and Jones W 1972 *Society of Naval Architects and Marine Engineers, and U.S. Navy, Advanced Marine Vehicles Meeting*, July 17, 1972
[11] Hanson R K, Spearrin R M and Goldenstein C S 2016 *Spectroscopy and Optical Diagnostics for Gases* (Cham: Springer International Publishing) pp. 107–130
[12] Park C S, Newfield M E, Fletcher D G, Gokcen T and Sharma S P 1998 *J. Thermophys. Heat Transf.* **23** 023001
[13] Donohue J, Fletcher D and Park C 1998 7*th AIAA/ASME Joint Thermophysics and Heat Transfer Conference*, July 15, 1998
[14] Park C, Newfield M, Fletcher D and Gokcen T 1998 36*th AIAA Aerospace Sciences Meeting and Exhibit*, January 12, 1998
[15] Laux C O, Spence T G, Kruger C H and Zare R N 2003 *Plasma Sources Sci. Technol.* **12** 125

[16] Hornkohl J O, Fleischmann J P, Surmick D M, Witte M J, Swafford L D, Woods A C and Parigger C G 2014 *J. Phys.: Conf. Ser.* **548** 012040
[17] Dikalyuk A, Kozlov P, Romanenko Y, Shatalov O and Surzhikov S 2013 *44th AIAA Thermophysics Conference*, July 24, 2013, San Diego, America
[18] Akatsuka H 2019 *Adv. Phys. X* **4** 1592707
[19] Cipullo A, Savino L, Marenna E and De Filippis F 2012 *Aerosp. Sci. Technol.* **23** 358
[20] Savino L, Cinquegrana D, French A, De Cesare M and Vecchio A D 2022 *J. Quant. Spectrosc. Ra.* **291** 108323
[21] Winter M and Prabhu D 2011 42*nd AIAA Thermophysics Conference*, June 27, 2011, Honolulu, America
[22] Koch H, Butler B, Winter M and Arnold C 2016 46*th AIAA Thermophysics Conference*, June 13, 2016, Washington, America
[23] Morin A J, Osborn R, Schindler J C, Jagun P, Fletcher D G and Meyers J M 2020 *AIAA Scitech 2020 Forum*, January 6, 2020, Orlando, America
[24] Dubuet U, Mariotto P, Perrin M and Laux C O 2021 *AIAA Scitech 2021 Forum*, January 1, 2021, Virtual Event
[25] Pietanza L D, Colonna G and Capitelli M 2023 *Plasma Phys. Contr. F* **65** 044004
[26] Ridenti M A, Reis J, Caliari F, Miranda F, Essiptchouk A and Filho G P 2024 *IEEE Transactions on Plasma Science* **52** 67
[27] Winter M, Srinivasan C and Charnigo R 2015 *46th AIAA Plasmadynamics and Lasers Conference*, June 22, 2015, Dallas, America
[28] Yu X, Peng J, Sun R, Yang X, Wang C, Sun J, Li X, Jia B, Zhao Y and Chen D 2012 *Opt. Lett.* **37** 2106
[29] Zhu W, Li X, Sun R, Cao Z,Yuan M, Sun L, Yu X and Wu J 2022 *Energy* **240** 122827
[30] Hu W, Yin K, Wang X, Yang J, Liu K, Peng Q and Xu Z 2023 *Chin. Phys. B* **32** 105201
[31] Han M, Yu X, Peng J, Yang C, Cao Z, Qi J, Yuan X 2025 *Spectrosc. Spect. Anal.*, **45** 947 (in Chinese)
[32] Winter M W, Srinivasan C, Charnigo R and Prabhu D K 2018 *J. Thermophys. Heat Tr.* **32** 1088
[33] De Giacomo A, Dell'Aglio M, Gaudiuso R, Amoruso S and De Pascale O 2012 *Spectrochim. Acta B: At. Spectrosc.* **78** 1
[34] Herzberg G 1953 *Molecular spectroscopy and molecular structure I.Spectra of Diatomic Molec* (New York: D.Van Nostrand Company) pp. 49
[35] Josyula E 2015 *Hypersonic Nonequilibrium Flows: Fundamentals and Recent Advances* (Reston: American Institute of Aeronautics and Astronautics, Inc.) p. 360
[36] Shi D, Xing W, Sun J, Zhu Z and Liu Y 2011 *Comput. Theor. Chem.* **966** 44
[37] Laux C O 2002 *von karman institute lecture series 2002 - 07*
[38] Laux C O 2008 *vki course on hypersonic entry and cruise vehicles*
[39] Specair v3.0 user manual. Preprint at http://specair-radiation.net/manual.php [2025]
[40] Wissler C 1905 *Science* **22** 309
[41] Xiao C, Ye J, Esteves R M and Rong C 2016 *Concurr. Comput. Pract. Exp.* **28** 3866
[42] Kumar N, Kumar P, Badagabettu S N, Lewis M G, Adiga M and Padur A A 2018 *Dermatol. Res. Pract.* **2018** 4512840
[43] Menke W 2015 *Surv. Geophys.* **36** 1
[44] Samuels K E and Baccarella D 2024 *AIAA SCITECH 2024 Forum*, January 4 2024